

RESEARCH ARTICLE | FEBRUARY 11 2022

Shock-induced spallation in a nanocrystalline high-entropy alloy: An atomistic study

Special Collection: Shock Behavior of Materials

Daniel Thürmer  ; Nina Gunkelmann  

 Check for updates

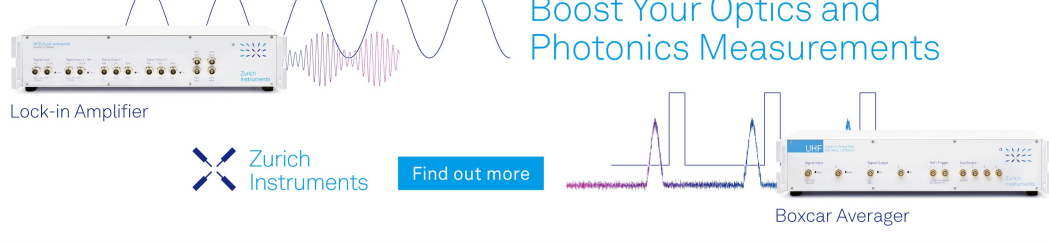
J. Appl. Phys. 131, 065902 (2022)

<https://doi.org/10.1063/5.0082199>



22 May 2024 17:11:22

Boost Your Optics and Photonics Measurements



Lock-in Amplifier

Zurich Instruments

Find out more

Boxcar Averager

Shock-induced spallation in a nanocrystalline high-entropy alloy: An atomistic study

Cite as: J. Appl. Phys. 131, 065902 (2022); doi: 10.1063/5.0082199

Submitted: 13 December 2021 · Accepted: 27 January 2022 ·

Published Online: 11 February 2022



View Online



Export Citation



CrossMark

Daniel Thürmer and Nina Gunkelmann ^{a)}

AFFILIATIONS

Division Computational Material Sciences/Engineering, Institute of Applied Mechanics, Arnold-Sommerfeld-Straße 6, 38678 Clausthal-Zellerfeld, Germany

Note: This paper is part of the Special Topic on Shock Behavior of Materials.

^{a)}**Author to whom correspondence should be addressed:** Nina.gunkelmann@tu-clausthal.de

ABSTRACT

High-entropy alloys are attracting an increasing interest due to their promising mechanical properties. However, their high-pressure properties are not fully understood. We study shock-induced spallation in a nanocrystalline high-entropy alloy using various grain sizes. Our results show that the spall strengths for the nanocrystals are significantly reduced in comparison to single crystals. In contrast to previous results on single crystals, we observe a large number of stacking faults, twins, and dislocations during the shock, which persist even during the release of the shock wave. This behavior is in good agreement with recent experiments of shock loading via high power lasers where pronounced nanotwinning has been observed in the recovered samples.

Published under an exclusive license by AIP Publishing. <https://doi.org/10.1063/5.0082199>

I. INTRODUCTION

High-entropy alloys (HEAs) consist of equiatomic mixtures of (usually) five or more elements and are attracting an increasing interest due to their promising material properties.^{1–5} Based on the used material, HEAs tend to have good ductility, corrosion resistance, and high yield strength. Pang *et al.* showed for the refractory high-entropy alloy (RHEA), Ti_{1.5}ZrNbAl_{0.3}, a good ductility with high yield strength, large plasticity, and specific yield strength-plasticity, thanks to solid solution strength and cross-slip of dislocations.⁶ Severe lattice distortion in NbTaTiVZr is also an important factor to achieve high strength in HEAs.⁷ The investigation of Qiu *et al.* of compositionally complex alloys, Al_xCoCrFeNiTi_y (CCA), in 0.6M NaCl showed good corrosion resistance in general. The dominant type of corrosion in that scenario is pitting based on microstructural analysis including XPS.⁸ Among them, one of the most studied HEAs is the Cantor alloy, which forms an equiatomic CoCrFeMnNi alloy⁹ in a single-phase face-centered cubic solid solution. HEAs are known to exhibit both high strength and ductility and their mechanical properties have been extensively studied.^{2,10–13} However, their high pressure properties are less explored. Jiang *et al.* conducted gas gun experiments of the Cantor alloy and demonstrated that the yield strength increased significantly with the strain

rate and exceeded the values for many austenitic steels.¹⁴ The formation of shear bands occurred only after extremely large shear strains, with exceptionally high fracture toughness under dynamic loading.² Recently, Zhao *et al.* have subjected CrMnFeCoNi HEAs to severe plastic deformation and observed dense structures comprising stacking faults, twins, and transformation from the face-centered cubic to the hexagonal close-packed structure and amorphization.¹⁵ Using *in situ* synchrotron radiation x-ray diffraction technique and high-resolution transmission electron microscopes, the effect of defects on structure evolutions in Al_{0.1}CoCrFeNi high-entropy alloys has been studied, showing that defects promote the phase transition from fcc to hcp.¹⁶

Atomistic simulations are capable of revealing important insights into the mechanical behavior of high-entropy alloys,^{17–21} including the influence of plasticity under compression and tension,²⁰ as well as indentation.¹⁸ Recent MD simulations of nanocrystalline samples of the Cantor alloy under tension²¹ show that mechanical twinning prevails as a deformation mechanism. In the preliminary work, we studied shock-induced spallation in the single crystal Cantor alloy and compared our results to experimental loading by high power lasers.²² Both experiments and simulations showed a very high spall strength.

However, most of recent atomistic studies in high-entropy alloys deal with fcc single crystals. For works on nanocrystalline HEAs, we can mention the paper by Li *et al.*, who studied the influence of temperature and the strain rate on plasticity in a nanocrystalline CoNiFeAlCu HEA.²³ Recently, the kinetics of strain induced phase transformation in single- and nanocrystalline HEAs has been evaluated.²⁴ To our knowledge, the effect of grain boundaries on spallation behavior in HEAs has not been considered before using MD simulations. This, however, could have a major impact because grain boundaries could lower the required spall stress.²⁵

In this paper, we, therefore, study shock-induced spallation in a nanocrystalline HEA using various grain sizes.

II. METHODS

The simulations performed in this paper were carried out by the public-domain molecular dynamics code LAMMPS developed by Sandia National Laboratories and Temple University.²⁶ The alloy used for the simulations is CoCrFeMnNi with randomly distributed atoms across the whole sample, containing 20% atoms of each element and having a lattice constant of $a_0 = 0.3595$ nm. The samples are of nanocrystalline nature with an fcc structure and a fixed number of grains, which are generated randomly and were constructed with a Voronoi construction algorithm.²⁷ We used three samples with different grain numbers in total for the simulations: 16 grains (four grains along the z direction and two grains along the lateral directions) with 1.91×10^6 atoms, 32 grains (eight grains along the z direction and two grains along the lateral directions) with 1.91×10^6 atoms, and 64 grains (16 grains along the z direction and two grains along the lateral directions) with 1.89×10^6 atoms. For 16, 32, and 64 grains, the average grain contains 27 421, 62 766, and 112 376 atoms corresponding to an average grain size of $(9 \times 9 \times 4.5)$, $(9 \times 9 \times 9)$, and $(9 \times 9 \times 18)$ nm. The measures for all samples are $18 \times 18 \times 72$ nm³ and the used potential for the simulation is based on the modified embedded-atom method (MEAM).¹⁹ The shock and recovery simulations were carried out using the NVE ensemble. Before we can run the simulations, we must relax the samples first. We subject the system first to energy minimization using the fire minimizer²⁸ followed by the conjugate gradient method (cg), and then to high-temperature annealing. Note that the fire minimization is significantly faster than standard implementations of the conjugate gradient method. The NPH ensemble is used for equilibration three times and the temperature is rescaled, while the shock and recovery simulations use an NVE ensemble. The initial pressure for the NPH ensemble is carried over from the cg style, runs for 2 ps, and is scaled to 700 K temperature well below the melting temperature. All pressure components in the x , y , and z directions are coupled. The next two NPH ensembles run for 100 ps each, while the temperature is 700 K for the first 100 ps and afterward slowly decreased to almost 0 K over the next 100 ps. The equilibration simulations run for 202 ps in total each. Note that there is no significant change in the equiatomic distribution at the grain boundaries after relaxation as has been observed from Monte Carlo simulations of the Cantor alloy.²⁹ A reason might be that the time scales here are considerably smaller such that segregation effects are less probable. Each sample is tested with three different velocities: 0.5, 0.8, and 1.6 km/s.

We induce shock waves in the sample by piston-driven simulation. The piston has a thickness of 0.3 nm and is accelerated into the z direction, while the velocity is increased linearly from zero to the shock velocity. The acceleration process for each simulation is defined as a loop, which is carried out for 0.2 ps in total. After the maximum velocity is reached, the simulation carries on for additional 20 ps to ensure that the profile of the shock wave is stable. Fig 1 shows the shock process of a sample with 32 grains at 1.6 km/s shock velocity for visualization. The sample is compressed in the z direction with the top end of the sample in a fixed position. The velocity and pressure are checked after the shock simulation to ensure the proper shock wave stability. Note that a large number of stacking faults, identified as the double layer of hcp, is observed during compression. In addition, some bcc atoms are discovered, which could be due to the significant uniaxial distortion of the fcc lattice and thermal noise. The recovery simulation is carried out afterward. The recovery simulations are started when the front of the shock wave is closest to the free surface at the end of the sample, at 11 ps for 0.5 km/s, 10 ps for 0.8 km/s, and 9 ps for 1.6 km/s, respectively.

The recovery simulation scripts have an integrated deceleration loop to reduce the piston velocity back to zero. This process takes 5 ps in total for each simulation. The simulation continues after the loop for at least an additional 30 ps. While some simulations ran longer than that, the important information is obtained in the 30 ps timeframe. This is based on the examination of single crystals²² in a similar simulation setup with 50 ps recovery time, and it turned out that the simulation time of 50 ps is too high. Failure generally occurred way before the simulation finished at 50 ps. This justified a reduction of the timeframe mentioned because the samples themselves have the same length and failure later than 30 ps is not to be expected. The obtained data from each sample is evaluated and key material properties will be examined and compared with each other. These material properties are the velocity in the z direction v_z , the stress in the z direction P_{zz} , and

22 May 2024 17:11:22

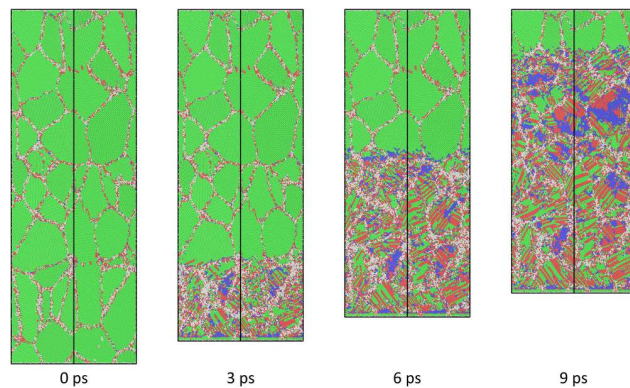


FIG. 1. Snapshots of the shock compression process at 0 (initial stage), 3, 6, and 9 ps, respectively. The sample has 32 grains and is compressed with an accelerated piston at a velocity of 1.6 km/s. The piston itself is visible as a small layer of atoms on the bottom of the sample. Green is fcc, red is hcp, blue is bcc, and gray is other structures.

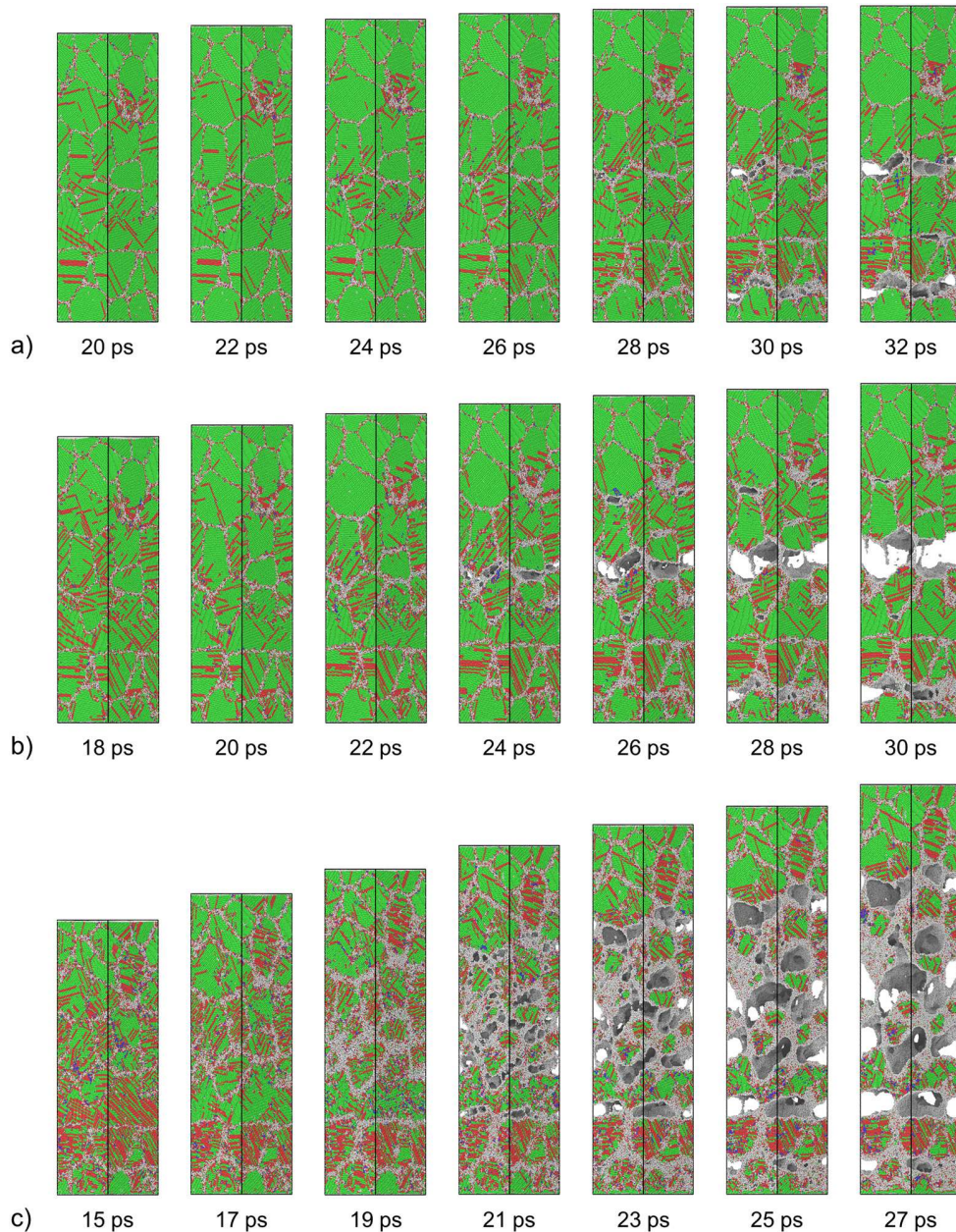
the shear stress. The shear stress is defined as follows:³⁰

$$P_{\text{shear}} = \frac{1}{2}(P_{zz} - P_{\text{trans}}), \quad (1)$$

with the transverse pressure defined as

$$P_{\text{trans}} = \frac{1}{2}(P_{xx} + P_{yy}). \quad (2)$$

P_{ij} describes the components of the stress tensor while the formulas calculate the shear stress. OVITO Pro³¹ is used to visualize the data, which includes graphs for v_z , P_{zz} , shear stress, and



22 May 2024 17:11:22

FIG. 2. Snapshots of the sample with 16 grains at 0.5 (a), 0.8 (b), and 1.6 km/s (c). The structures are identified with OVITO using PTM. Green is fcc, red is hcp, blue is bcc, and gray is other structures. The shock wave propagated from bottom to top.

Polyhedral Template Matching (PTM) with RMSD = 0.2, which is used to identify structures in each sample.

Different shock wave velocities (SWVs) for different grain numbers and shock velocities are also calculated using the visualized data from OVITO Pro. Two different points in time during

the shock process form the basis for the calculations, 5 and 9 ps. The same points are chosen for each shock velocity and grain number for good comparability between each other: the beginning of the shock front. The difference in the distance traveled at 5 and 9 ps is then divided by the time difference of 4 ps.

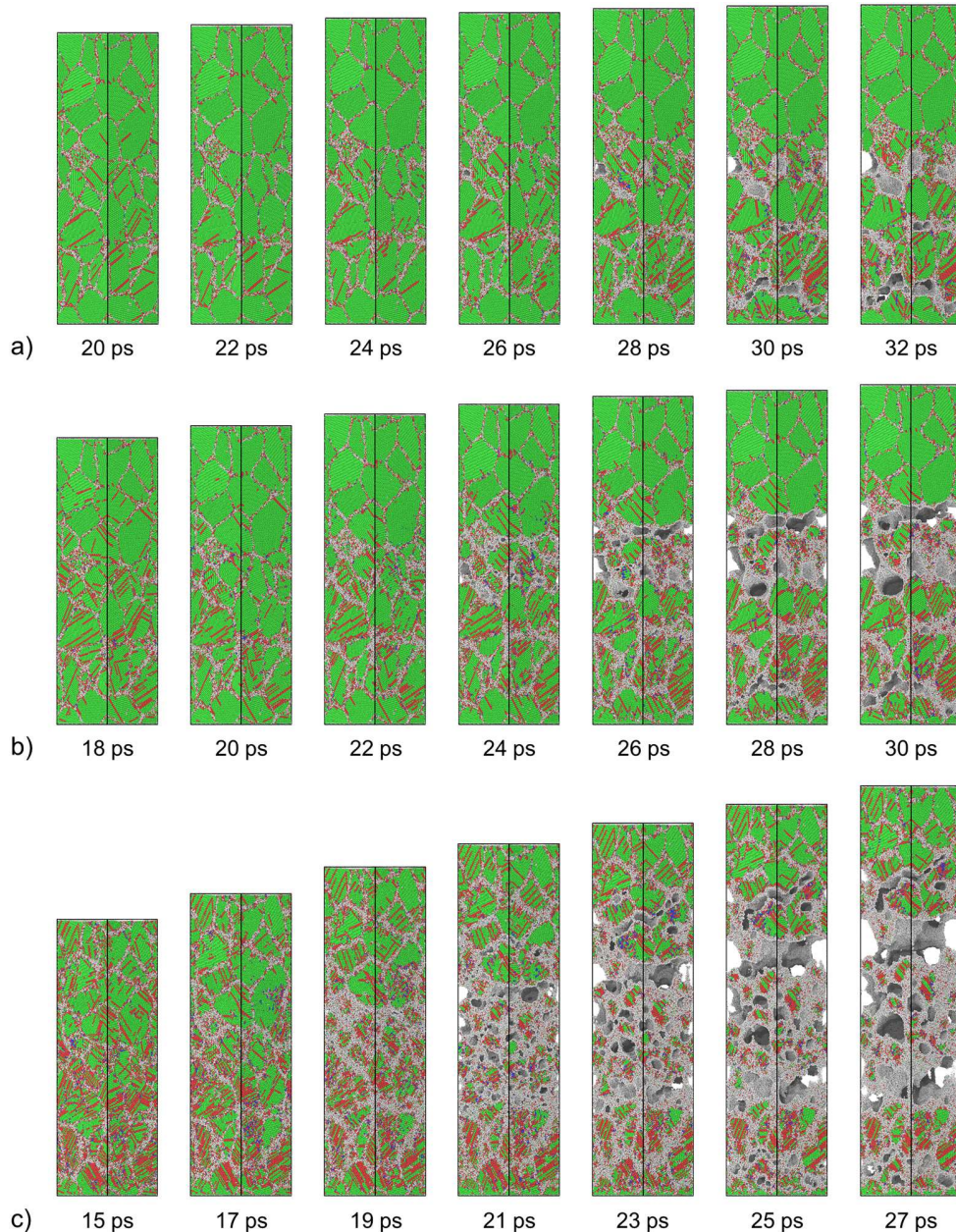


FIG. 3. Snapshots of the sample with 32 grains at 0.5 (a), 0.8 (b), and 1.6 km/s (c). The structures are identified with OVITO using PTM. Green is fcc, red is hcp, blue is bcc, and gray is other structures. The shock wave propagated from bottom to top.

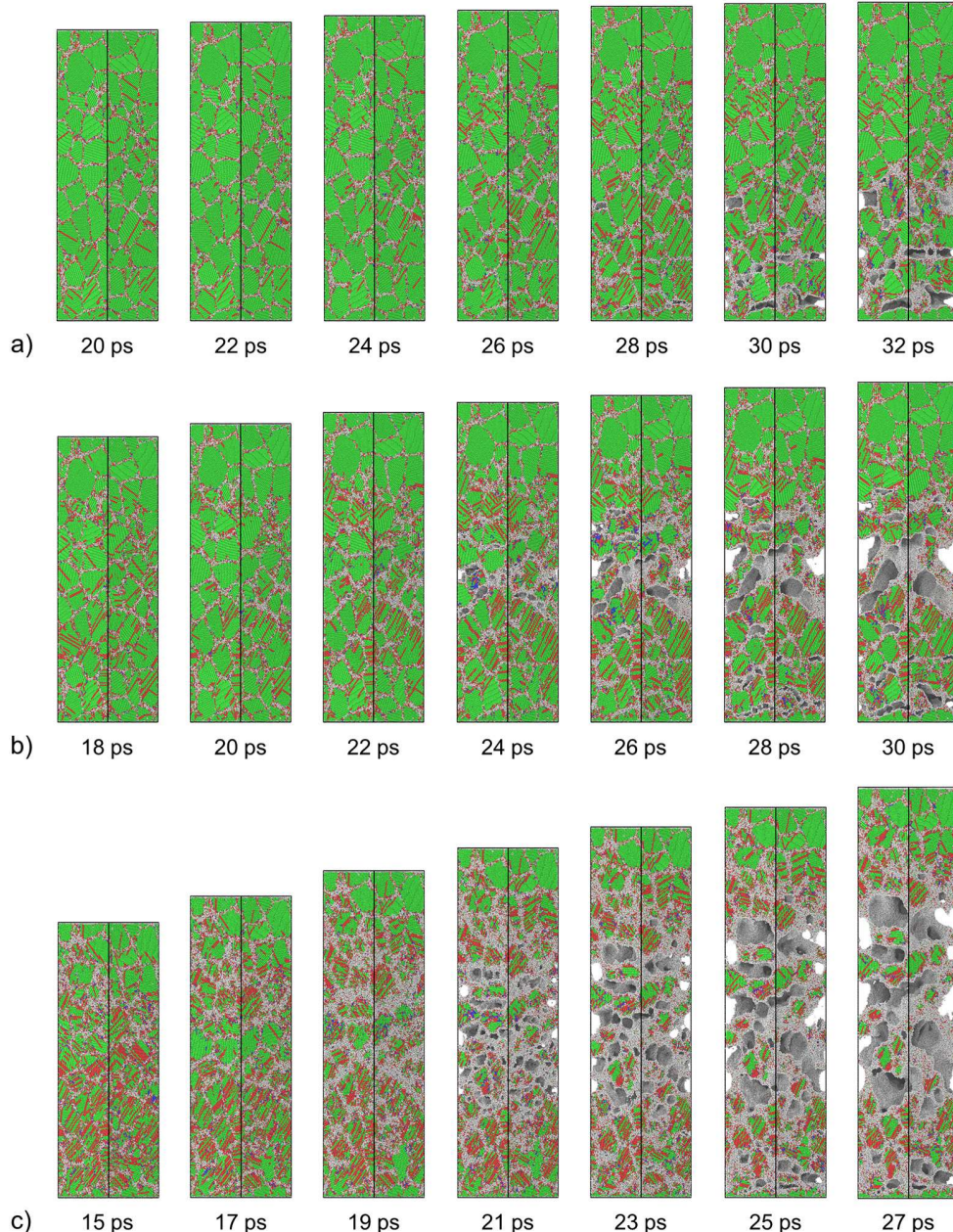
22 May 2024 17:11:22

III. RESULTS

A. Microstructural changes

When a shock wave reaches the free surface of the target, it reflects as a release wave and the superposition results in a tensile

pulse. Spall occurs when the magnitude of the tensile stress surpasses a certain value. Figures 2–4 display the changes induced in our sample by the passage of the shock and release wave for different piston velocities for our MD simulations using samples with 16, 32, and 64 grains. The spallation process begins at the surface



22 May 2024 17:11:22

FIG. 4. Snapshots of the sample with 64 grains at 0.5 (a), 0.8 (b), and 1.6 km/s (c). The structures are identified with OVITO using PTM. Green is fcc, red is hcp, blue is bcc, and gray is other structures. The shock wave propagated from bottom to top.

as a succession of tiny voids along the grain boundaries. Then, amorphization of the intergranular regions where the voids were nucleated occurs. Recently, amorphous phase transformations in an ultrafine-grained Cantor alloy have also been revealed from *in situ* straining TEM experiments.³² No voids are formed in the grain interior. In general, the spall surface appears to be more smooth for the cases with larger grain sizes. For stronger shock waves, many cracks are visible and spall occurs at multiple nucleation sites, while in the case of our weakest shock, spall is concentrated in the center of the sample. Similar behavior has also been shown for single crystals.²² We recognize a large number of stacking faults, twins, and dislocations during the recovery process. Note that stacking faults are detected as a double layer of hcp atoms, while twin boundaries appear as a single layer of hcp atoms. However, in comparison to the material behavior for single crystals, it can be seen that these dominate the microstructure even after the sample has broken, whereas for single crystals most dislocations and twins disappeared during release. The behavior observed here is in better agreement with the experiments where plasticity has been observed in the TEM of recovered samples.²² Here, pronounced nanotwinning has been observed in the recovered experimental sample.

B. Property profiles

We also see in the profiles of the velocity along the shock direction, the pressure component parallel to the shock direction, and the shear stress (Figs. 5–7 for 16, 32, and 64 grains) that the grains have a significant influence on the shock wave propagation through the sample. Our earlier paper showed a uniform and well defined shock front for single crystals,²² while this is not the case for nanocrystals. Shear stress occurs close to the shock front independent of shock velocity, although the velocity itself has an influence on the profile. While the profiles for 0.5 km/s are more uniform for the shear stress at 11 ps, for 0.8 km/s shock velocities, we observe a small peak close to the shock fronts at 10 ps. At 1.6 km/s, there are clear visible spikes regardless of grain number. It is worth mentioning that the number of grains itself seems to have an influence as well. The 16-grain sample has the roughest shear stress profile for 0.5 km/s at 11 ps with a dip in the pressure profile at around 35 nm depth in the z direction and a bulge in the velocity profile at the same position. The rough shear stress profile is also seen at 0.8 km/s at 10 ps but with a small peak close to the shock front of roughly 4.3 GPa stress. The dip in the pressure profile and bulge in the velocity profile remains unchanged. At

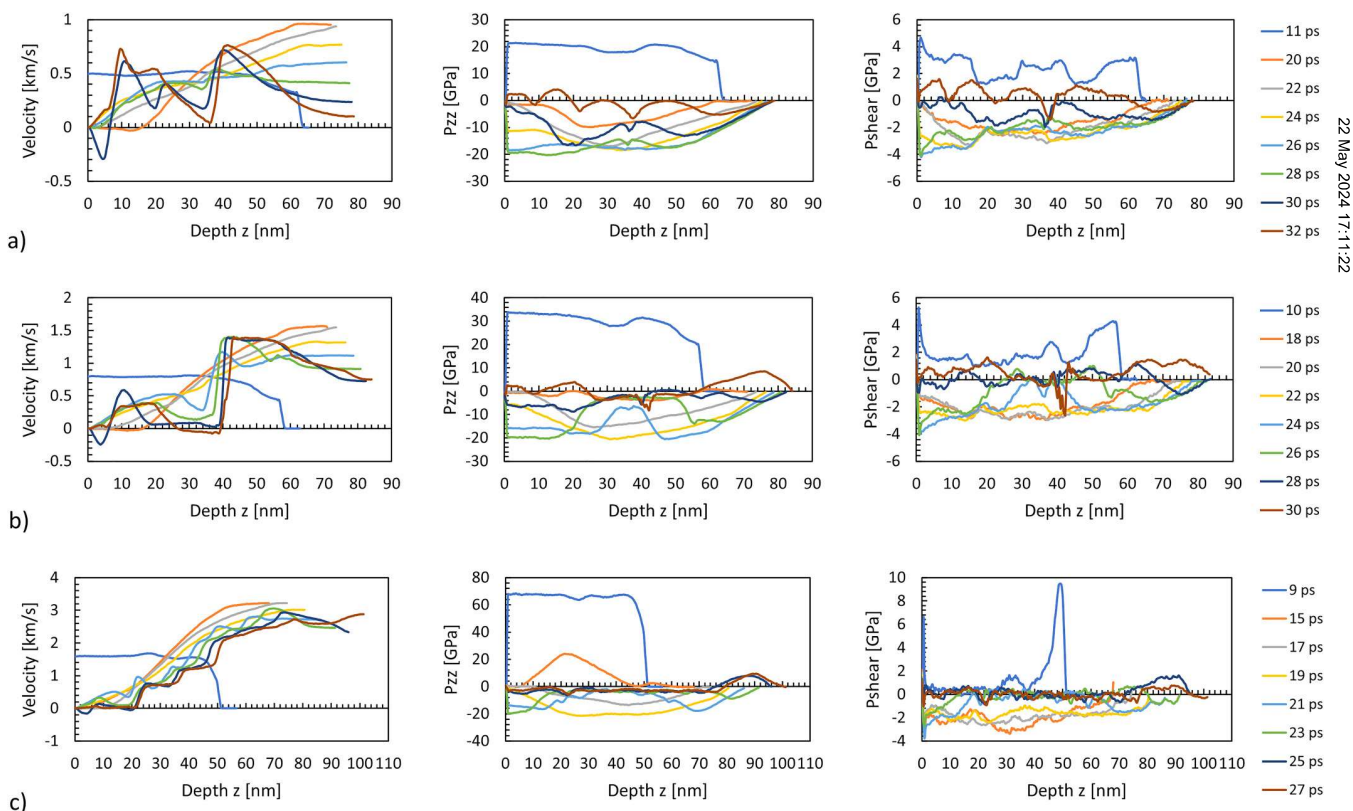


FIG. 5. Spatial profiles of the atom velocity in the z direction, v_z , the pressure components parallel to the shock wave propagation direction, P_{zz} , and the shear stress for the sample with 16 grains for several piston velocities: 0.5 (a), 0.8 (b), and 1.6 km/s (c).

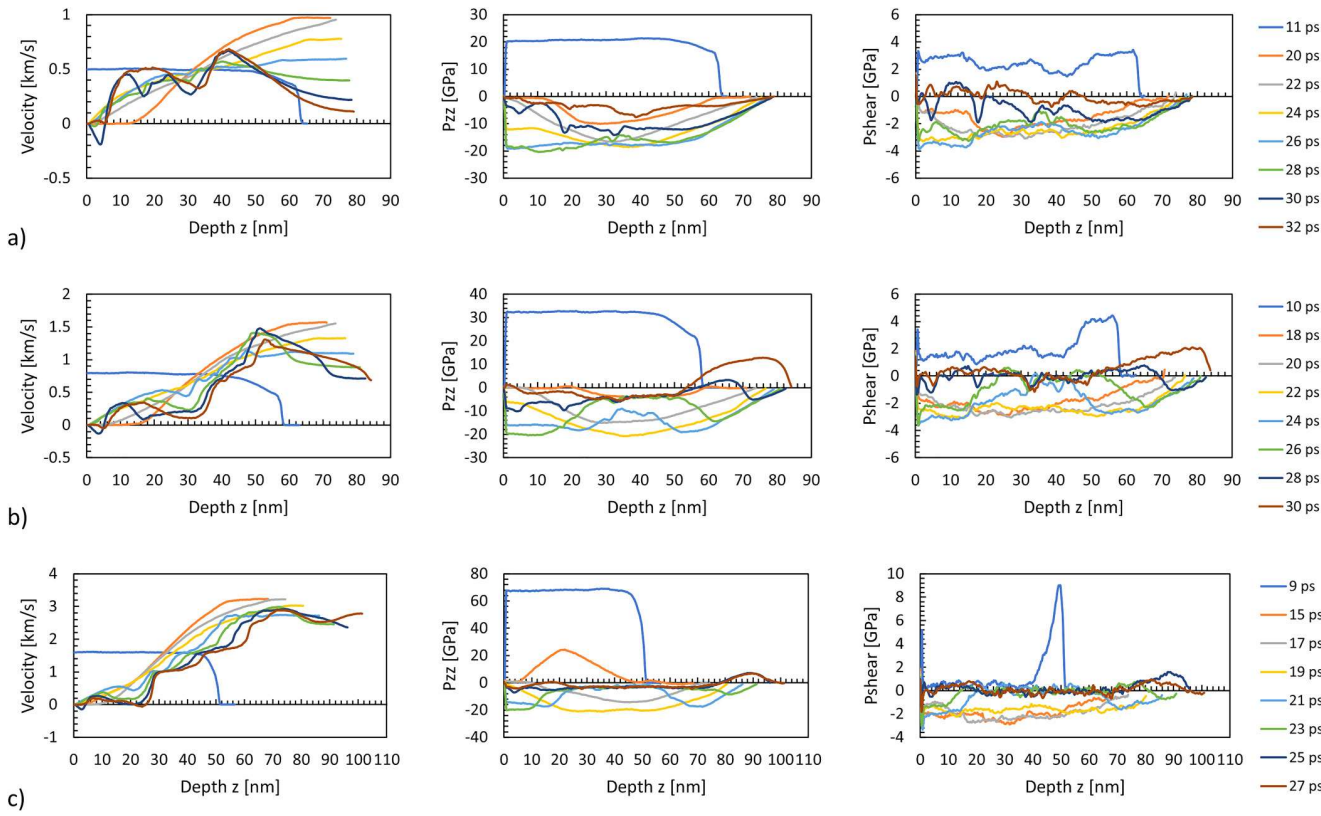


FIG. 6. Spatial profiles of the atom velocity in the z direction, v_z , the pressure components parallel to the shock wave propagation direction, P_{zz} , and the shear stress for the sample with 32 grains for several piston velocities: 0.5 (a), 0.8 (b), 1.6 km/s (c).

22 May 2024 17:11:22

1.6 km/s at 9 ps the shear stress shows a spike of around 9.5 GPa at roughly 50 nm, while there is a clear drop-off in pressure and velocity at around the same depth in the z direction. There is a small dip in the pressure profile at around 25 nm and a bulge in the velocity profile at the same position. The 32-grain sample shows a smoother shear stress profile at 0.5 km/s at 11 ps compared to the 16-grain sample. The shear stress profile for 0.8 km/s at 10 ps shows a small peak as it does for the 16-grain sample with the same velocity, but the peak is a bit higher at roughly 4.4 GPa. At 1.6 km/s at 9 ps, the spike of the shear stress reaches around 9 GPa. As with the 16-grain sample, the pressure and velocity curves fall off, while the shear stress rises drastically at 50 nm. The 64-grain sample has the smoothest shear stress profile at 0.5 km/s at 11 ps but is still comparable to the 32-grain sample. The peak of the shear stress profile at 0.8 km/s 10 ps is at 5.1 GPa. The spike at 1.6 km/s at 9 ps of the shear stress is lowest at 7.8 GPa. The pressure and velocity curves fall off, while the shear stress rises at \sim 50 nm here as well.

C. Spall stress

Table I shows the maximum (or minimum depending on context) pressure P_{zz} when the sample starts to fail based on the

velocity and grain number. This is called the spall stress. The influence of the different grain numbers is lower than the influence of velocity. At 0.5 km/s, the sample starts to fail after 24 ps runtime, at 0.8 km/s at 22 ps runtime, and at 1.6 km/s at 19 ps simulation runtime. Thus, the spall time decreases with increasing piston velocities as a consequence of the increase in the shock wave speed with the piston speed. Increasing the velocity leads to an increase of P_{zz} regardless of grain numbers but there is a visible trend.

A sample with a larger number of grains shows a lower spall strength compared to a sample with less grains. In fact, the trend seems to be consistent with increasing velocity except for 0.8 km/s with 16 and 32 grains. An increase in grains from 16 to 32 showed a small increase of the spall strength instead of a decrease. The values of the spall strengths for the nanocrystals are significantly reduced in comparison to single crystals where values of almost \sim 30 GPa have been reached.²² This is expected because grain boundaries usually lower the required spall stress as observed in Ta.²⁵ Here, an increase in spall stress with increasing grain sizes was observed²⁵ in agreement with our result. Note that the relative decrease in the spall strength from single to nanocrystal is larger than for bcc³³ and fcc single crystals.³⁴ This might be related to the presence of twins in the HEA structure, which are persistent unlike for single crystals. These

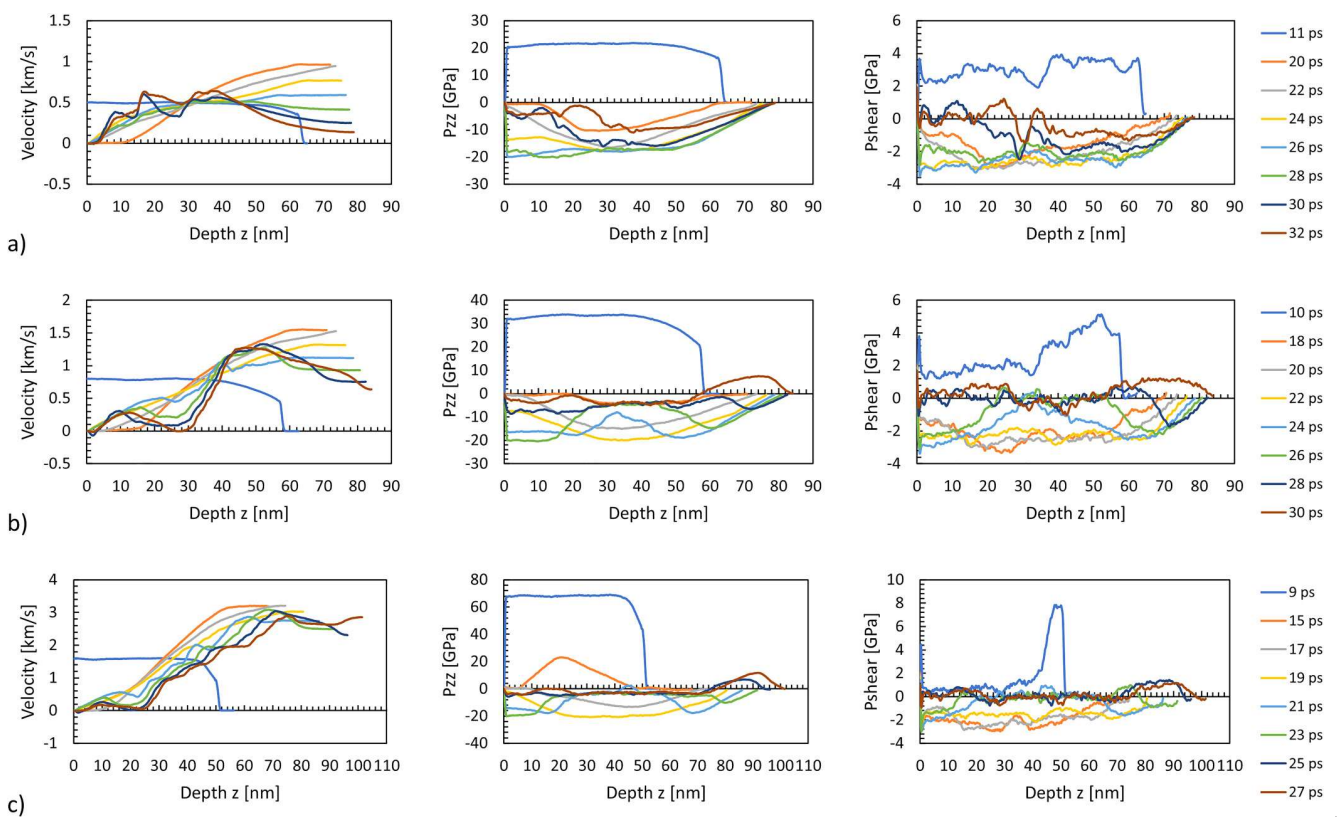


FIG. 7. Spatial profiles of the atom velocity in the z direction, v_z , the pressure components parallel to the shock wave propagation direction, P_{zz} , and the shear stress for the sample with 64 grains for several piston velocities: 0.5 (a), 0.8 (b), 1.6 km/s (c).

22 May 2024 17:11:22

preserved twins are known to have large influence on the spall strength in single crystals.^{35,36} However, other influencing factors, such as the dependence on the deformation rate and segregation effects, would have to be studied here. Despite the reduction of spall stress for nanocrystals, spallation stresses of up to 21 GPa are still remarkably high. Note that the reason for the higher spall stress at

increased piston velocities is the larger strain rate which is known to lead to larger spall stresses.^{21,37,38}

D. Shock wave velocities

Table II shows the shock wave velocities for the shock velocities and grain numbers used in this paper. The shock wave

TABLE I. Different nanocrystal samples at 24 ps for 0.5 km/s, 22 ps for 0.8 km/s and 19 ps for 1.6 km/s and their P_{zz} values (spall strength) depending on grain number. Beginning of failure occurred at the given points in time.

0.5 km/s shock velocity at 24 ps			
Grains	16	32	64
P_{zz} (GPa)	18.5	18.5	18.2
0.8 km/s shock velocity at 22 ps			
Grains	16	32	64
P_{zz} (GPa)	20.5	20.7	19.9
1.6 km/s shock velocity at 19 ps			
Grains	16	32	64
P_{zz} (GPa)	21.3	20.9	20.7

TABLE II. Different shock wave velocities (SWVs) depending on grain numbers and shock velocity of the piston itself.

0.5 km/s shock velocity			
Grains	16	32	64
SWV (km/s)	6.1	6.0	6.2
0.8 km/s shock velocity			
Grains	16	32	64
SWV (km/s)	6.3	6.2	6.4
1.6 km/s shock velocity			
Grains	16	32	64
SWV (km/s)	7.0	6.9	7.2

velocities are significantly higher compared to the shock velocities, which is to be expected.³⁹ For 0.5 km/s, the velocities are in the range of 6.0–6.2 km/s; for 0.8 km/s, in the range of 6.2–6.4 km/s; and for 1.6 km/s, in the range of 6.9–7.2 km/s. Increasing the shock velocity leads to an increase in shock wave velocity, although the effect itself seems to be small compared to the relative increase in shock velocity. Similar results have been found for Fe single and polycrystals.^{39,40} The influence of the grain numbers is relatively small, although it is worth mentioning that the shock wave velocity for 32 grains seems to be the lowest for every shock velocity.

IV. CONCLUSION

In this paper, we have presented molecular dynamics simulations of shock wave loading and spall in the nanocrystalline equiatomic Cantor high-entropy alloy, FeCrMnNiCo. We observe that the spall strength is around ~ 21 GPa at $\sim 10^9$ s $^{-1}$ which is smaller than values of ~ 30 GPa at $\sim 10^9$ s $^{-1}$ found in our previous work for single crystals. In contrast to the results on single crystals, we observe a large number of stacking faults, twins and dislocations during the shock which even persists during the release of the shock wave. This is in good agreement to experiments where significant plasticity has been found in the recovered samples. As expected, the spall stress decreases with decrease in grain size. The high spalling resistance observed here is due to the homogeneous composition of the alloy, which clearly has no second phase particles and/or segregations at the grain boundaries.

ACKNOWLEDGMENTS

We greatly appreciate the financial support from Simulation Science Center Clausthal/Göttingen.

AUTHOR DECLARATIONS

Conflict of Interest

The authors have no conflicts of interest to declare.

DATA AVAILABILITY

The data that support the findings of this study are available from the corresponding author upon reasonable request.

REFERENCES

- ¹D. B. Miracle and O. N. Senkov, "A critical review of high entropy alloys and related concepts," *Acta Mater.* **122**, 448–511 (2017).
- ²Z. Li, S. Zhao, R. O. Ritchie, and M. A. Meyers, "Mechanical properties of high-entropy alloys with emphasis on face-centered cubic alloys," *Prog. Mater. Sci.* **102**, 296–345 (2019).
- ³Y. Zhou, D. Zhou, X. Jin, L. Zhang, X. Du, and B. Li, "Design of non-equiatomic medium-entropy alloys," *Sci. Rep.* **8**, 1236 (2018).
- ⁴E. P. George, D. Raabe, and R. O. Ritchie, "High-entropy alloys," *Nat. Rev. Mater.* **4**, 515–534 (2019).
- ⁵W. Li, D. Xie, D. Li, Y. Zhang, Y. Gao, and P. Liaw, "Mechanical behavior of high-entropy alloys," *Prog. Mater. Sci.* **118**, 100777 (2021).
- ⁶J. Pang, H. Zhang, L. Zhang, Z. Zhu, H. Fu, H. Li, A. Wang, Z. Li, and H. Zhang, "Ductile Ti_{1.5}ZrNbAl_{0.3} refractory high entropy alloy with high specific strength," *Mater. Lett.* **290**, 129428 (2021).
- ⁷C. Lee, Y. Chou, G. Kim, M. C. Gao, K. An, J. Brecht, C. Zhang, W. Chen, J. D. Poplawsky, G. Song, Y. Ren, Y.-C. Chou, and P. K. Liaw, "Lattice-distortion-enhanced yield strength in a refractory high-entropy alloy," *Adv. Mater.* **32**, 1–9 (2020).
- ⁸Y. Qiu, S. Thomas, D. Fabijanic, A. J. Barlow, H. L. Fraser, and N. Birbilis, "Microstructural evolution, electrochemical and corrosion properties of Al_xCoCrFeNiTi_y high entropy alloys," *Mater. Des.* **170**, 107698 (2019).
- ⁹B. Cantor, I. Chang, P. Knight, and A. Vincent, "Microstructural development in equiatomic multicomponent alloys," *Mater. Sci. Eng. A* **375–377**, 213–218 (2004).
- ¹⁰E. George, W. Curtin, and C. Tasan, "High entropy alloys: A focused review of mechanical properties and deformation mechanisms," *Acta Mater.* **188**, 435–474 (2020).
- ¹¹Y. Zhang, T. T. Zuo, Z. Tang, M. C. Gao, K. A. Dahmen, P. K. Liaw, and Z. P. Lu, "Microstructures and properties of high-entropy alloys," *Prog. Mater. Sci.* **61**, 1–93 (2014).
- ¹²Y. Lu, X. Gao, L. Jiang, Z. Chen, T. Wang, J. Jie, H. Kang, Y. Zhang, S. Guo, H. Ruan, Y. Zhao, Z. Cao, and T. Li, "Directly cast bulk eutectic and near-eutectic high entropy alloys with balanced strength and ductility in a wide temperature range," *Acta Mater.* **124**, 143–150 (2017).
- ¹³M. Wang, Y. Lu, T. Wang, C. Zhang, Z. Cao, T. Li, and P. K. Liaw, "A novel bulk eutectic high-entropy alloy with outstanding as-cast specific yield strengths at elevated temperatures," *Scri. Mater.* **204**, 114132 (2021).
- ¹⁴Z. J. Jiang, J. Y. He, H. Y. Wang, H. S. Zhang, Z. P. Lu, and L. H. Dai, "Shock compression response of high entropy alloys," *Mater. Res. Lett.* **4**, 226–232 (2016).
- ¹⁵S. Zhao, Z. Li, C. Zhu, W. Yang, Z. Zhang, D. E. J. Armstrong, P. S. Grant, R. O. Ritchie, and M. A. Meyers, "Amorphization in extreme deformation of the CrMnFeCoNi high-entropy alloy," *Sci. Adv.* **7**, eabb3108 (2021).
- ¹⁶R. Li, Y. Ma, X. Liu, Y. Lu, Y. Zhang, P. Yu, and G. Li, "Effect of defects on the phase transition of Al_{0.1}CoCrFeNi high-entropy alloy under high pressure," *Intermetallics* **140**, 107388 (2022).
- ¹⁷L. Xie, P. Brault, A.-L. Thomann, and J.-M. Bauchire, "AlCoCrCuFeNi high entropy alloy cluster growth and annealing on silicon: A classical molecular dynamics simulation study," *Appl. Surf. Sci.* **285**, 810–816 (2013).
- ¹⁸I. Alabd Alhafez, C. J. Ruestes, E. M. Bringa, and H. M. Urbassek, "Nanoindentation into a high-entropy alloy—An atomistic study," *J. Alloys Compds* **803**, 618–624 (2019).
- ¹⁹W.-M. Choi, Y. H. Jo, S. S. Sohn, S. Lee, and B.-J. Lee, "Understanding the physical metallurgy of the CoCrFeMnNi high-entropy alloy: An atomistic simulation study," *npj Comput. Mater.* **4**, 1 (2018).
- ²⁰Q. Fang, Y. Chen, J. Li, C. Jiang, B. Liu, Y. Liu, and P. K. Liaw, "Probing the phase transformation and dislocation evolution in dual-phase high-entropy alloys," *Int. J. Plast.* **114**, 161–173 (2019).
- ²¹Y. Qi, X. Chen, and M. Feng, "Molecular dynamics-based analysis of the effect of temperature and strain rate on deformation of nanocrystalline CoCrFeMnNi high-entropy alloy," *Appl. Phys. A* **126**, 529 (2020).
- ²²D. Thürmer, S. Zhao, O. R. Deluigi, C. Stan, I. A. Alhafez, H. M. Urbassek, M. A. Meyers, E. M. Bringa, and N. Gunkelmann, "Exceptionally high spallation strength for a high-entropy alloy demonstrated by experiments and simulations," *J. Alloys Compd.* **895**, 162567 (2022).
- ²³Z. Li, Y. Gao, S. Zhan, H. Fang, and Z. Zhang, "Molecular dynamics study on temperature and strain rate dependences of mechanical properties of single crystal Al under uniaxial loading," *AIP Adv.* **10**, 075321 (2020).
- ²⁴J. Li, Q. Fang, B. Liu, and Y. Liu, "Transformation induced softening and plasticity in high entropy alloys," *Acta Mater.* **147**, 35–41 (2018).
- ²⁵T. Remington, E. Hahn, S. Zhao, R. Flanagan, J. Mertens, S. Sabbaghianrad, T. Langdon, C. Wehrenberg, B. Maddox, D. Swift, B. Remington, N. Chawla, and M. Meyers, "Spall strength dependence on grain size and strain rate in tantalum," *Acta Mater.* **158**, 313–329 (2018).
- ²⁶S. Plimpton, "Fast parallel algorithms for short-range molecular dynamics," *J. Comput. Phys.* **117**, 1–19 (1995).
- ²⁷A. Frøseth, H. Van Swygenhoven, and P. Derlet, "Developing realistic grain boundary networks for use in molecular dynamics simulations," *Acta Mater.* **53**, 4847–4856 (2005).

- ²⁸E. Bitzek, P. Koskinen, F. Gähler, M. Moseler, and P. Gumbsch, "Structural relaxation made simple," *Phys. Rev. Lett.* **97**, 170201 (2006).
- ²⁹P. Wymblatt and D. Chatain, "Modeling grain boundary and surface segregation in multicomponent high-entropy alloys," *Phys. Rev. Mater.* **3**, 054004 (2019).
- ³⁰D. Tramontina, P. Erhart, T. Germann, J. Hawreliak, A. Higginbotham, N. Park, R. Ravelo, A. Stukowski, M. Suggit, Y. Tang, J. Wark, and E. Bringa, "Molecular dynamics simulations of shock-induced plasticity in tantalum," *High Energy Density Phys.* **10**, 9–15 (2014).
- ³¹A. Stukowski, "Visualization and analysis of atomistic simulation data with OVITO—The open visualization tool," *Model. Simul. Mater. Sci. Eng.* **18**, 015012 (2010).
- ³²H. Wang, D. Chen, X. An, Y. Zhang, S. Sun, Y. Tian, Z. Zhang, A. Wang, J. Liu, M. Song, S. P. Ringer, T. Zhu, and X. Liao, "Deformation-induced crystalline-to-amorphous phase transformation in a CrMnFeCoNi high-entropy alloy," *Sci. Adv.* **7**, eabe3105 (2021).
- ³³E. N. Hahn, T. C. Germann, R. J. Ravelo, J. E. Hammerberg, and M. A. Meyers, "On the ultimate tensile strength of tantalum," *Acta Mater.* **126**, 313–328 (2017).
- ³⁴A. M. Dongare, A. M. Rajendran, B. LaMattina, M. A. Zikry, and D. W. Brenner, "Atomic scale studies of spall behavior in nanocrystalline Cu," *J. Appl. Phys.* **108**, 113518 (2010).
- ³⁵K. Mackenchery, R. R. Valisetty, R. R. Namburu, A. Stukowski, A. M. Rajendran, and A. M. Dongare, "Dislocation evolution and peak spall strengths in single crystal and nanocrystalline Cu," *J. Appl. Phys.* **119**, 044301 (2016).
- ³⁶E. N. Hahn, S. J. Fensin, T. C. Germann, and G. T. Gray, "Orientation dependent spall strength of tantalum single crystals," *Acta Mater.* **159**, 241–248 (2018).
- ³⁷S. Razorenov, G. Kanel, A. Savinykh, and V. Fortov, "Large tensions and strength of iron in different structure states," *AIP Conf. Proc.* **845**, 650 (2006).
- ³⁸S. G. Srinivasan, M. I. Baskes, and G. J. Wagner, "Atomistic simulations of shock induced microstructural evolution and spallation in single crystal nickel," *J. Appl. Phys.* **101**, 043504 (2007).
- ³⁹N. Gunkelmann, D. R. Tramontina, E. M. Bringa, and H. M. Urbassek, "Interplay of plasticity and phase transformation in shock wave propagation in nanocrystalline iron," *New J. Phys.* **16**, 093032 (2014).
- ⁴⁰K. Kadau, T. C. Germann, P. S. Lomdahl, R. C. Albers, J. S. Wark, A. Higginbotham, and B. L. Holian, "Shock waves in polycrystalline iron," *Phys. Rev. Lett.* **98**, 135701 (2007).